

A discretization-convergent Level-Set-DEM

Shai Feldfogel¹, Konstantinos Karapiperis², Jose Andrade³,
and David S. Kammer¹

¹Institute for Building Materials, ETH, Zurich, Switzerland

²Department of Mechanical and Process Engineering, ETH,
Zurich, Switzerland

³Department of Mechanical and Civil Engineering, Caltech,
Pasadena, California, USA

October 3, 2022

Abstract

The recently developed level-set-DEM is able to seamlessly handle arbitrarily shaped grains and their contacts through a discrete level-set representation of grains' volume and a node-based discretization of their bounding surfaces. Heretofore, the convergence properties of LS-DEM with refinement of these discretizations have not been examined. Here, we examine these properties and show that the original LS-DEM diverges upon surface discretization refinement due to its force-based discrete contact formulation. Next, we fix this issue by adopting a continuum-based contact formulation wherein the contact interactions are traction-based, and show that the adapted LS-DEM is fully discretization convergent. Lastly, we discuss the significance of convergence in capturing the physical response, as well as a few other convergence-related topics of practical importance.

1 Introduction

Representing realistically-shaped grains has been a long-standing challenge in the Discrete Element Method (DEM) [9, 1, 12, 4, 2]. The Level-Set-Discrete-Element-Method (LS-DEM) was developed a few years ago to address this challenge [10, 8], and it has since been applied to study various granular systems made up of realistically shaped grains. Kawamoto et al. [8] simulated a triaxial compression test of Martian-like sand based on X-ray computed tomography of the actual grains used in the experiments. Karapiperis et al. [7] investigated the constitutive elasto-plastic response and shape effects upon loading and unloading of Hostun sand. Karapiperis et al. [6] studied the effects of reduced gravity on the strength of sand. Harmon et al. [3] studied the effects of brittle particle breakage in the context of realistic particles going through a Jaw crusher, in an odeometric set-up, and in wall demolition. Karapiperis et al. [5] studied the formation and evolution of stress transmission paths in entangled granular assemblies, and their macroscopic mechanical properties.

LS-DEM's ability to represent arbitrarily shaped grains and resolve contact between such grains is due to two discretizations - a node-based discretization of grain boundary and a discretized Level-Set representation of grain volume. The refinement of the surface discretization (SD) is defined by the distance between surface nodes and it determines the accuracy with which the contact regions are spatially resolved. The refinement of the volume discretization (VD) is defined by the step size of the volume grid on which the Level-Set is calculated, and it determines the accuracy with which the magnitude and the direction of the penetration at a contact node are evaluated.

Convergence upon discretization refinement is important because it assures that results are discretization independent and quantitatively meaningful. It is therefore a common requirement from discretization-based numerical models such as the Finite Difference Methods and the Finite Element Method (FEM). In this study, we address of the convergence properties of

the discretization-based LS-DEM, which have not yet been addressed in the literature.

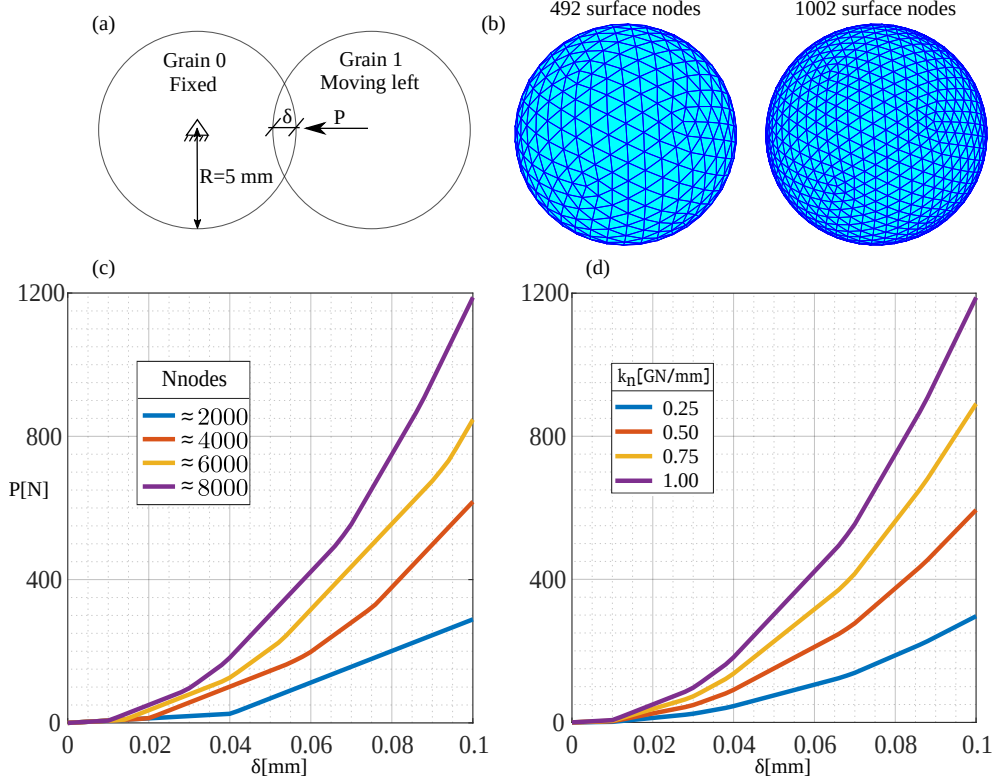


Figure 1: Two-sphere central-compression with original LS-DEM: (a) Configuration; (b) two surface discretizations; (c) P - δ curves diverge in the original LS-DEM (d) mesh refinement equivalent to increasing k_n .

The convergence of LS-DEM upon SD refinement is considered in Fig 1. Fig. 1(a) depicts a case of central-compression between two-spheres. P and δ denote the compression force and the penetration depth, respectively. Fig. 1(b) shows two SDs differing in the total number of surface nodes (Nnodes). As in all the examples in this study, the surface of the grains is represented by a triangle mesh, whose nodes constitute the SD. Fig. 1(c) shows P - δ curves from four analyses with a different Nnodes. Fig. 1(d) shows P - δ curves from analyses with Nnodes=8,000 and with four linearly-spaced values of the

penalty parameter k_n . Fig. 1(c) shows that the response scales approximately linearly with SD refinement, which means that LS-DEM diverges upon SD refinement. Fig. 1(d) shows that the response also scales approximately linearly with k_n , implying that SD refinement is equivalent to increasing k_n .

The divergent behavior observed in Fig. (c) underscores the need to adapt LS-DEM so that it becomes discretization convergent and it raises several questions of interest:

1. Why does LS-DEM divergence upon SD refinement, and how can this divergence be fixed?
2. How does the relation between the SD and VD refinements affect convergence?
3. What is the physical significance of convergence in terms of correctly capturing the mechanical response?

The main objectives of the present study are to fix LS-DEM's divergence issue and to address these questions.

Next, in section 2 we identify the cause for LS-DEM divergence and propose an adapted contact formulation that eliminates this divergence. In section 3, we examine the convergence properties of the adapted formulation upon SD refinement and address the aforementioned open questions. We summarize the study in Section 4.

2 Methodology

The reason why the original LS-DEM diverges upon SD refinement is discussed in Sec. 2.1; The elimination of this divergence is described in 2.2; The adapted formulation is detailed in 2.3.

2.1 Why does the original LS-DEM diverge?

The root cause of LS-DEM's divergent behavior observed in Figure 1(a) is that the inter-grain penetration stiffness, which controls the global strength and stiffness, scales linearly with the number of surface nodes.

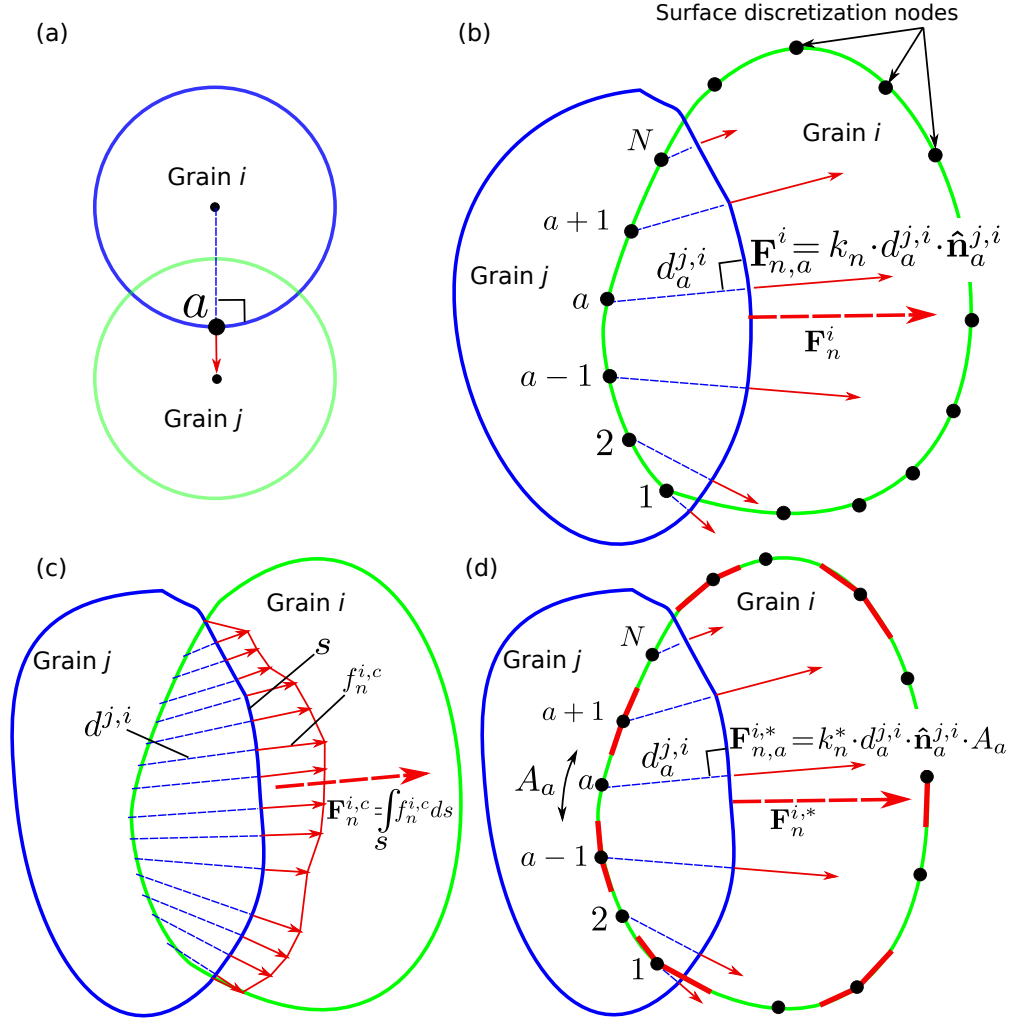


Figure 2: The adapted LS-DEM overcomes the divergent behavior of the original LS-DEM by adopting a continuum-based contact description: (a) ordinary DEM; (b) original LS-DEM; (c) continuum contact model; and (d) adapted LS-DEM (penetrations are grossly exaggerated for illustrative purposes)

To see this in more detail, consider Fig. 2. In ordinary DEM, the grains are spherical and each contact comprises a single penetration point a as illustrated in Fig 2(a). In LS-DEM, due to the surface discretization, there

are generally multiple contact nodes between two contacting grains, as shown in Figure 2(b). At each node, the normal force acting on grain i by grain j is, similarly to ordinary DEM:

$$\mathbf{F}_{n,a}^i = k_n \cdot d_a^{j,i} \cdot \hat{\mathbf{n}}_a^{j,i} \quad (1)$$

where k_n is the normal penalty parameter with dimensions [force/penetration], $d_a^{j,i}$ and $\hat{\mathbf{n}}_a^{j,i}$ denote, respectively, the penetration depth and the unit normal to grain j at penetration point a , and where the summation is carried over the surface nodes on the boundary of grain j .

The resultant normal force \mathbf{F}_n^i acting on grain i by grain j , marked in Fig. 2 by a dashed arrows, is the of vector sum of nodal forces over the N contact nodes:

$$\mathbf{F}_n^i = \sum_{a=1}^N \mathbf{F}_{n,a}^i = \sum_{a=1}^N k_n \cdot d_a^{j,i} \cdot \hat{\mathbf{n}}_a^{j,i} \quad (2)$$

Then, defining the average penetration $\bar{d}_a^{j,i} \equiv \frac{\sum_{a=1}^N d_a^{j,i}}{N}$ and the grain penetration stiffness k^{grain} as $\frac{|\mathbf{F}_n^i|}{\bar{d}_a^{j,i}}$, it follows that k^{grain} is linear in both N and k_n :

$$k^{grain} \equiv \frac{|\mathbf{F}_n^i|}{\bar{d}_a^{j,i}} = \frac{\sum_{a=1}^N |k_n \cdot d_a^{j,i} \cdot \hat{\mathbf{n}}_a^{j,i}|}{\frac{\sum_{a=1}^N d_a^{j,i}}{N}} = N \cdot k_n \cdot \frac{\sum_{a=1}^N |d_a^{j,i} \cdot \hat{\mathbf{n}}_a^{j,i}|}{\sum_{a=1}^N d_a^{j,i}} = N \cdot k_n \quad (3)$$

The distinction between the grain penetration stiffness k^{grain} which refers to interaction between grains as a whole and the normal penalty parameter k_n which refers to contact interactions at the node level does not exist in ordinary DEM. There, $N=1$ and k^{grain} and k_n are therefore one and the same.

The linearity of k^{grain} with k_n in Eq. (3) is reflected in Fig. 1(b), and it is common to all DEM variants. It is useful because it allows to calibrate k_n as a correlate of the elastic modulus. In contrast, the linearity of k^{grain} with N is unique to LS-DEM and it is problematic because, as the SD is refined, N and k^{grain} increase proportionally, leading to the divergence observed in Fig. 1(a).

2.2 How we eliminate LS-DEM's divergence

The key to fixing LS-DEM's divergence is to eliminate the discretization dependence of the penetration stiffness expressed in Eq. (3). To do that, we adopt the continuum-based approach described in Figure 2(c), where contact forces are integrals of surface tractions over the contact area s , rather than sums of nodal forces. The dimensions of the continuum-based penalty parameter k_n^* are those of an elastic foundation [traction/penetration], differently from k_n 's [force/penetration]. This approach provides the resultant normal force $\mathbf{F}_n^{i,c}$ and the commensurate penetration stiffness k^{grain} , with the necessary linkage to and bounding by the finite contact area s , bounding which the original formulation expressed in Equation (2) lacks.

The continuum-based resultant normal force $\mathbf{F}_n^{i,c}$ reads:

$$\mathbf{F}_n^{i,c} = \int_s d\mathbf{F}_n^{i,c} \quad (4)$$

where the superscript c denotes the continuum-based approach, s denotes the contact area between the grains, and the elemental $d\mathbf{F}_n^{i,c}$ reads:

$$d\mathbf{F}_n^{i,c} = \mathbf{f}_n^{i,c} ds = k_n^* \cdot d^{j,i} \cdot \hat{\mathbf{n}}^{j,i} ds \quad (5)$$

where $\mathbf{f}_n^{i,c}$ are the normal tractions, $d^{j,i}$ the normal penetrations, and $\hat{\mathbf{n}}^{j,i}$ the surface normals.

We evaluate the integral in Equation (4) numerically as a sum of nodal contributions at contacting nodes, as illustrated in Fig. 2(d). The resultant normal force in the adapted LS-DEM $\mathbf{F}_n^{i,*}$ therefore reads:

$$\mathbf{F}_n^{i,*} = \sum_{a=1}^N \mathbf{F}_{n,a}^{i,*} \quad (6)$$

where the superscript * denotes the adapted formulation. The nodal normal force $\mathbf{F}_{n,a}^{i,*}$, which is the finite analog of $d\mathbf{F}_n^{i,c}$ from Equation (5), reads:

$$\mathbf{F}_{n,a}^{i,*} = k_n^* \cdot d_a^{j,i} \cdot \hat{\mathbf{n}}_a^{j,i} \cdot A_a \quad (7)$$

where A_a is the tributary area of node a , see Fig. 2(d).

The penetration stiffness $k^{int,*}$ in the adapted model then reads:

$$k^{int,*} \equiv \sum_{a=1}^N \frac{|\mathbf{F}_{n,a}^{i,*}|}{d_a^{j,i}} = \sum_{a=1}^N \frac{|k_n^* \cdot d_a^{j,i} \cdot \hat{\mathbf{n}}_a^{j,i} \cdot A_a|}{d_a^{j,i}} = \sum_{a=1}^N k_n^* \cdot A_a = k_n^* \cdot N \cdot A_a \quad (8)$$

The "corrective" factor A_a and the elastic-foundation nature of k_n^* are the two keys to resolving the divergence issue. By taking A_a equal to the total surface area of the grain divided by the total number of surface nodes, an increase in N with SD refinement is off-set ("corrected") by a proportional decrease in A_a , so that the sensitivity of $k^{int,*}$ on the SD becomes minor, and the global response converges upon SD refinement, as will be shown in the next section.

The tangential contact formulation requires a treatment similar to that of the normal contact formulation, for similar reasons. Comparing Eqs. (1) and (7), the modification of the normal nodal force in the adapted formulation amounts to replacing k_n with the $k_n^* \cdot A_a$. The modification of the nodal tangential force in the adapted formulation is analogous to this replacement. In the original LS-DEM (see Equation (15) in [8]), the elastic tangential force at node a , which is the basis for the commonly-used Coulomb friction law, is based on the product $k_s \cdot \Delta \mathbf{S}_a$, where k_s [force/displacement] is the tangential stiffness analogous to k_n and where $\Delta \mathbf{S}_a$ is the (incremental) tangential slip vector analogous to the penetration vector $d_a^{j,i} \cdot \hat{\mathbf{n}}_a^{j,i}$. Hence, the modification of the nodal shear force amounts to replacing k_s with $k_s^* \cdot A_a$, where the distributed tangential stiffness k_s^* has dimensions [traction/penetration].

2.3 Adapted LS-DEM formulation

With the modifications to the contact formulation described above, the adapted LS-DEM's formulation is neatly obtained from the original one by replacing k_n and k_s in Equations (5) and (9) from [8] with $k_n^* \cdot A_a$ and $k_s^* \cdot A_a$, respectively. Regarding the computational aspect, it is pointed out that the additional computational cost in the adapted formulation is effectively zero. It consists merely of calculating A_a once for each node in the pre-processing stage and appending it to k_n^* and k_s^* whenever the node is in contact.

3 Results and discussion

The convergence properties of the adapted LS-DEM in different configurations are evaluated and discussed in sections 3.1-3.2. The other questions posed at the end of the Introduction are addressed in sections 3.3-3.4.

3.1 Two-sphere central-compression

We begin the evaluation of the adapted LS-DEM's convergence properties by revisiting the two-sphere configuration described in Fig. 1. Fig. 3(a) depicts five $P - \delta$ curves obtained with the adapted LS-DEM and with the same SD's as those used for Fig. 1(c). The $P - \delta$ curves in Fig. 3(a) show that, in contrast to the divergent behavior of the original LS-DEM seen in Fig. 3(c), the adapted formulation converges upon SD refinement. Fig. 3(b) shows the linearity of the response with k_n^* , reflecting the linearity of $k^{int,*}$ with k_n^* in accordance with Eq. (8). The convergence of the adapted formulation and the linearity of the response with k_n^* in accordance with Eq. (8) show that cause of divergence has indeed been correctly identified and eliminated as described in Sec. 2.

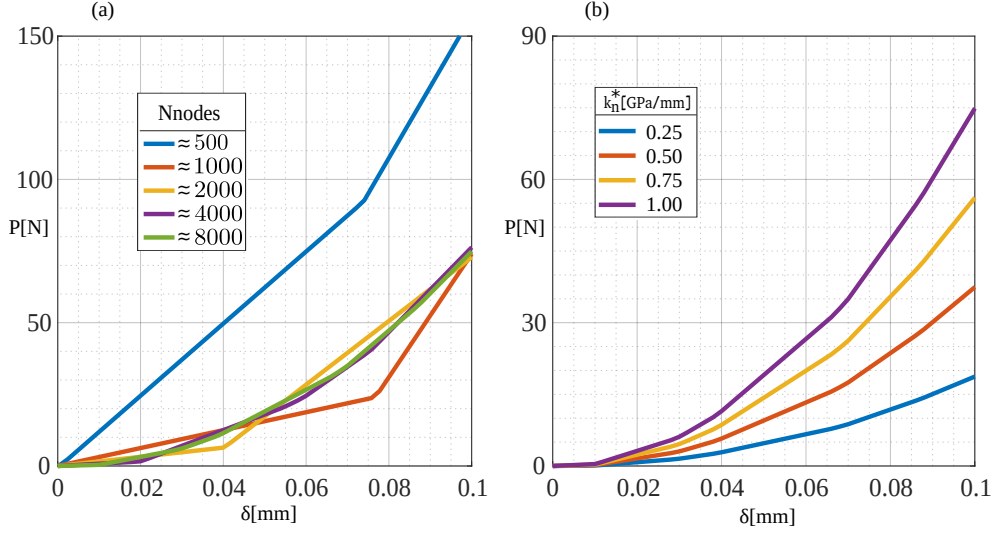


Figure 3: The two-sphere central-compression case with the adapted LS-DEM: (a) the P - δ curves converge upon SD refinement; (b) the response scales linearly with k_n^* in accordance with Eq. (8).

3.2 A topologically interlocked slab

Moving on from the simple two-sphere case to a more realistic configuration with multiple particles, we consider next the topologically interlocked slabs studied experimentally in [11]. Topologically interlocked slabs are made of un-bonded building blocks that hold together by contact and friction thanks to their interlocking shapes. Their analysis with LS-DEM represents the latter's novel application to structural analysis problems, where convergence is particularly important.

Fig. 4(a) shows a typical planar-faced block that makes up the interlocking slab and its cross-sections in the xz and yz planes. The bottom face of the block is a square with side length $l = 8.33$ mm, and the angle of inclination of its sloping lateral faces is $\theta = 2.5^\circ$. Fig. 4(b) shows the basic 5-block interlocked cell formed by surrounding a block by four similar ones rotated with respect to it by 90° with respect to the z axis. Fig. 4(c) shows the entire slab with the contour of a basic cell around the central block marked

in black. The slabs' dimensions are 50 x 50 x 3.18 mm, and they consist of boundary blocks that are fixed by an external constraint along the edges and of internal blocks. Fig. 4(d) shows the triangular mesh constitutes the SD of the central block.

The slab was loaded by a concentrated load P in the negative z direction. The load was affected by prescribing a constant velocity to a spherical loading indenter with a 2.5 mm radius. P and the corresponding displacement δ are indicated by a yellow arrow in the negative z direction in Figure 4(c). Prior to the indentation loading phase, the assembly was subjected to gravity until it reached a relaxed state, i.e., until the kinetic energy lowered to effectively zero. The relaxed positions and rotations of the blocks were taken as the initial conditions for the concentrated load phase. The material density was taken equal to $2.5 \cdot 10^{-6} \frac{kg}{mm^3}$, and a friction coefficient $\mu=0.23$ was used, in accordance with [11].

Fig. 4(e) shows $P - \delta$ curves corresponding to four analyses made with the original LS-DEM, using $k_n=2$ GN/mm. Fig. 4(f) shows $P - \delta$ curves obtained with the most refined surface discretization (Nnodes=68,000) and a set of four evenly-spaced k_n 's. Fig. 4(a) shows that the $P - \delta$ curves scale linearly with both Nnodes and k_n , similarly to the two-sphere example shown in Fig. 1. Fig. 4(g) shows three $P - \delta$ obtained with the adapted LS-DEM for varying Nnodes between 17,000-68,000 and $k_n^*=2$ GPa/mm. Fig. 4(h) shows three $P - \delta$ obtained with the adapted LS-DEM, Nnodes=68,000, and a set of four linearly spaced k_n^* 's. From the essential overlapping of the three curves in Fig. 4(g) it is clear that the adapted LS-DEM converges with less than Nnodes=17,000. A fuller illustration of the convergence process is shown and discussed later in relation to Fig. 5. From Fig. 4(h), the response in the adapted formulation scales linearly with k_n^* , in accordance with Eq. (8).

Comparing Figs. 3(c,d) and 3(a,b) to Figs. 4(c,d,e,f), respectively, shows that, in both the two-sphere case and the slab example, the dependence of the original and adapted formulations of Nnodes, k_n , and k_n^* is essentially

the same. This means that neither the divergent nature of the original formulation nor the convergence of the adapted one dependent on the number on grains (blocks) in the problem.

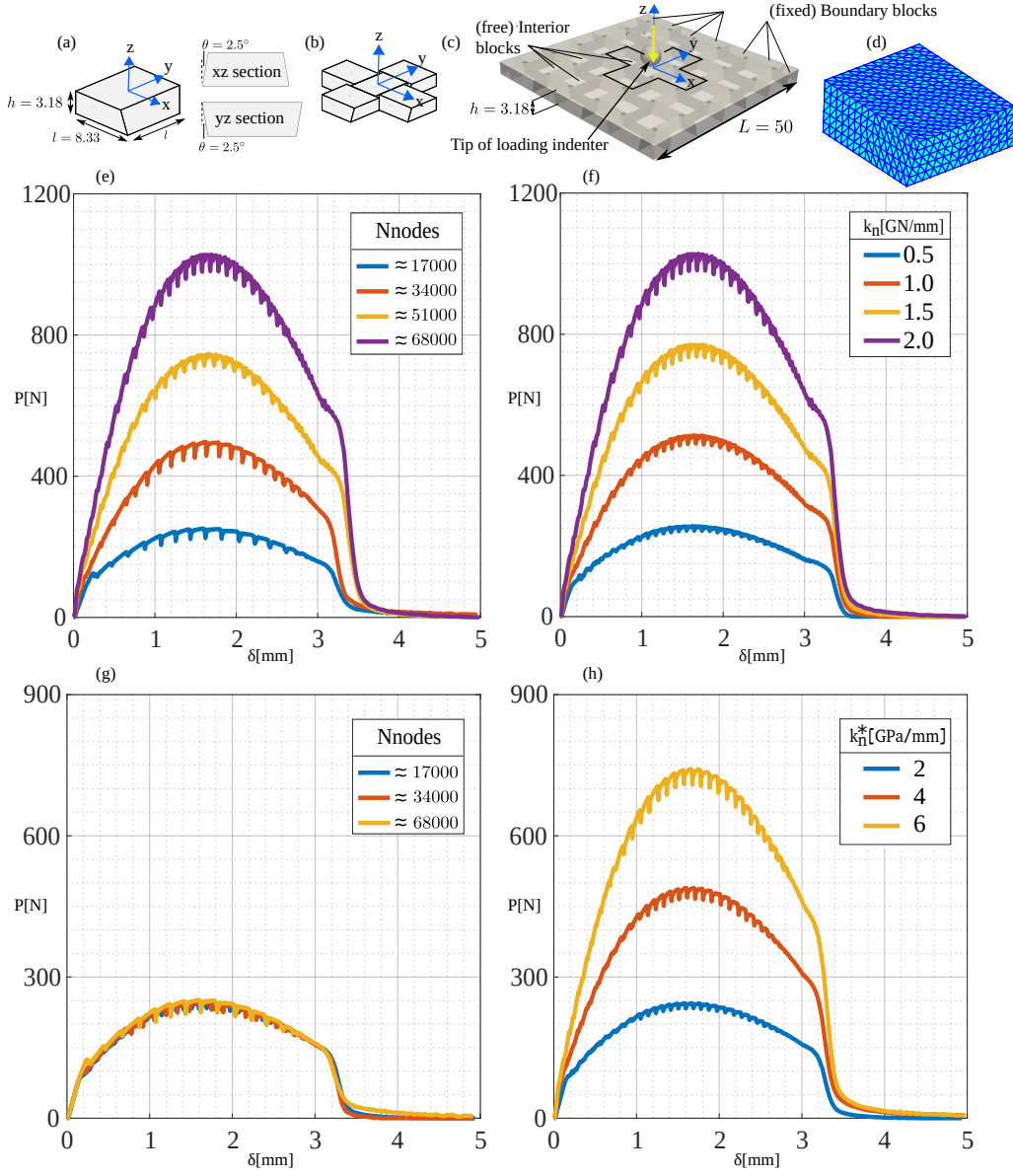


Figure 4: Topologically interlocked slab: (a-d) Configuration; (e-h) P - δ curves diverge in the original LS-DEM (e) and converge in the adapted LS-DEM (g) upon discretization refinement; the response scales linearly with the penalty parameters k_n and k_n^* (f,h).

3.3 The relation between SD and VD refinement

In the context of the original LS-DEM, it is not clear how to determine the relation between the SD refinement and the VD refinement. The convergence of the adapted LS-DEM provides a clear-cut criterion for this determination, namely that the SD and VD should be refined such that the results do not change with further refinement of either or both together. Going through such a two-way convergence study could provide a general estimate to how refined the SD should be relative to the VD. To obtain such an estimate, we consider next the two-way SD-VD convergence in the context of the topologically interlocked slab discussed in section 3.2.

Fig. 5(a,b) depict the two-way SD-VD convergence. Here, we choose the distance between surface nodes as the surface discretization parameter SDP, and the step size in the Level-Set volume grid as the volume discretization parameter VDP. The reason is that length parameters are a more meaningful measure for quantifying the relation between the SD and VD refinement than the number of nodes, which scales differently for SD and VD with the overall lineal dimensions of the grain.

Fig. 5(a) shows $P - \delta$ obtained for a series of SDP's at a constant VDP=0.025 mm. Considering the negligible differences between the two most refined analyses, SDP=0.06 mm (with Nnodes=68,314) was deemed the converged SDP. We note that the maximal P varies by a factor of approximately 2 as Nnodes grows by more than 2 orders of magnitude, from 420 with SDP=0.68 mm to 68,314 with SDP=0.06 mm. This speaks to the small sensitivity of the adapted formulation on the SD refinement, which allows to obtain reasonable estimates of the converged behavior with computationally cheaper coarse SDs. Fig. 5(b) shows $P - \delta$ obtained for a series of VDP's at a constant converged SDP=0.06 mm. Considering the negligible differences between the two most refined analyses, VDP=0.06 mm was deemed the converged SDP.

The fact that the response reached saturation with discretization refinement at SDP=0.06 mm and VDP=0.025 mm allows defining the VDP to

SDP ratio $\frac{0.025}{0.06} = 0.416$ required for convergence. This ratio may serve as a first-order approximation to facilitate future two-way SD-VD convergence studies.

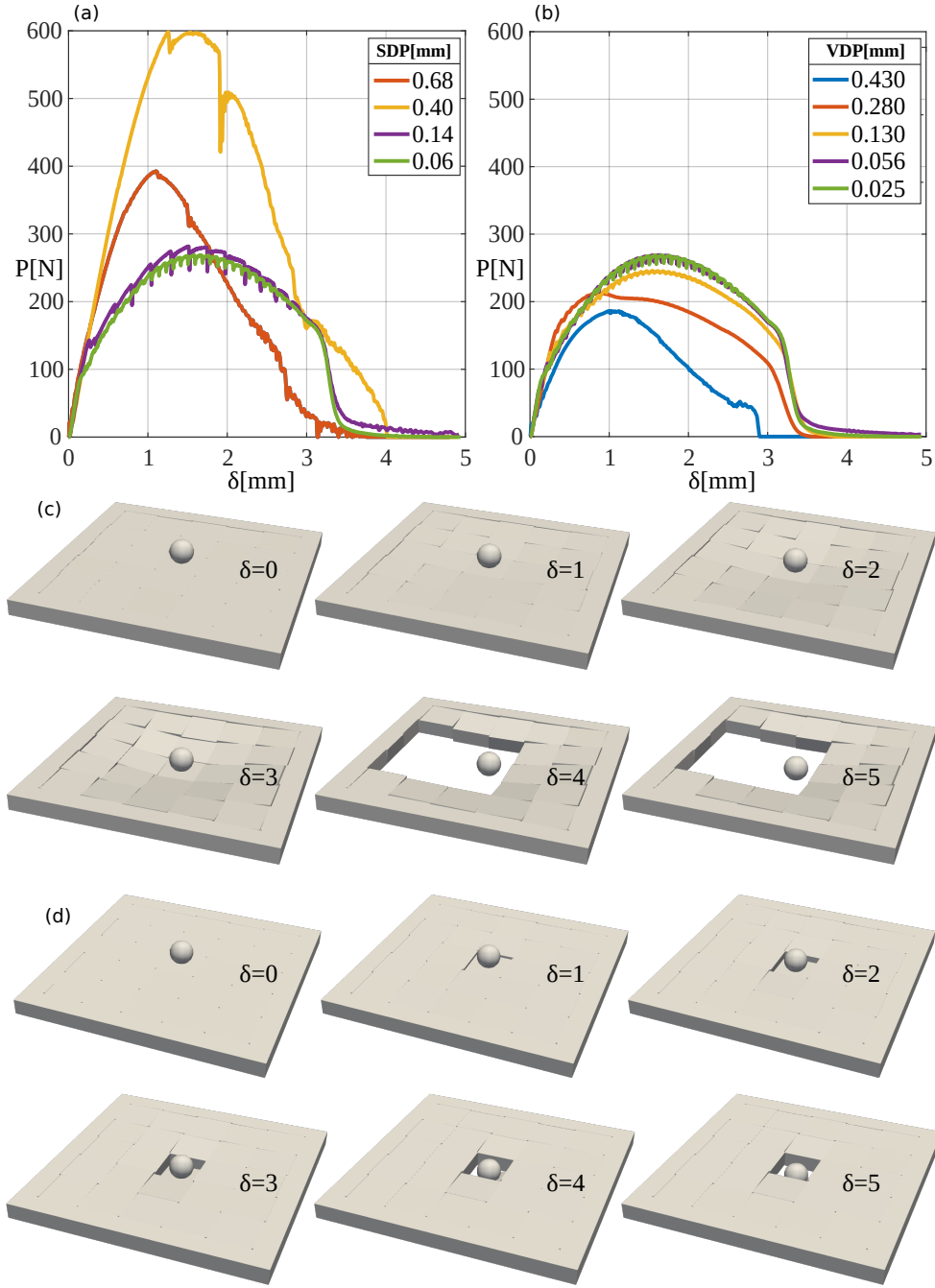


Figure 5: The adapted LS-Dem is fully discretization convergent: $P - \delta$ curve convergence with surface (a) and volume (b) discretization refinement; failure mechanism convergence from coarse (c) to refined (d) discretizations

3.4 The physical significance of convergence

How important is it to use a converged discretization in terms of correctly capturing the mechanical response? We address this question in the context of the topologically interlocked slabs by comparing the failure mechanism as obtained with the adapted LS-DEM to the experimentally observed one in [11]

In [11], the failure was governed by sliding of the central block and its eventual falling off. The failure mechanisms as obtained with the adapted LS-DEM are depicted in Figs. 5(c,d), through six snapshots corresponding to $\delta = 0, 1, \dots, 5$ mm. Fig. 5(c) shows that with the coarse discretization (SDP=0.68 mm and VDP=0.43 mm), the failure mechanism is qualitatively different from the experimentally observed one. The blocks stick to one another throughout most of the response and several of the central blocks end up falling-off. In contrast, Fig. 5(d) shows that the converged discretization correctly captures the experimentally observed failure. This speaks to the importance of having a converged LS-DEM formulation and working with converged discretizations for capturing the correct mechanical response.

4 Summary and outlook

In this paper, we have shown that the original LS-DEM diverges upon surface discretization refinement, even in a simple case of central compression between two spheres. We have further shown that this divergence is due to the force-based formulation of nodal contact interactions and the commensurate linear scaling of the grain penetration stiffness with the number of contacting surface nodes. Based on this, we have replaced the original contact formulation with a continuum-based one wherein the nodal contact interactions are traction-based. We have shown that the adapted LS-DEM is fully discretization convergent in different kinds of applications including the novel application of LS-DEM to structural analysis. Based on full two-way convergence study for the surface and the volume discretizations, we have de-

rived the volume-to-surface degree of refinement necessary for convergence, and we have shown the discretization convergence is physically significant in that it is necessary to correctly capture the mechanical response. The convergent nature of the adapted formulation paves the way to broaden the scope of LS-DEM applications to structural analysis of structures made of discrete building blocks. In such applications, the divergence of the original LS-DEM is most pronounced and therefore the convergence of the adapted LS-DEM is essential to obtain quantitatively meaningful results. Lastly, the fact that the additional computational cost of the adapted formulation is effectively zero, warrants its general use in future LS-DEM applications.

References

- [1] J.F. Favier et al. “Shape representation of axi-symmetrical, non-spherical particles in discrete element simulation using multi-element model particles”. In: *Engineering Computations* 16.4 (Jan. 1999). Publisher: MCB UP Ltd, pp. 467–480. ISSN: 0264-4401. DOI: 10.1108/02644409910271894. URL: <https://doi.org/10.1108/02644409910271894> (visited on 09/14/2022).
- [2] Y.T. Feng and D.R.J. Owen. “A 2D polygon/polygon contact model: algorithmic aspects”. In: *Engineering Computations* 21.2/3/4 (Jan. 2004). Publisher: Emerald Group Publishing Limited, pp. 265–277. ISSN: 0264-4401. DOI: 10.1108/02644400410519785. URL: <https://doi.org/10.1108/02644400410519785> (visited on 08/09/2022).
- [3] John M. Harmon, Daniel Arthur, and José E. Andrade. “Level set splitting in DEM for modeling breakage mechanics”. en. In: *Computer Methods in Applied Mechanics and Engineering* 365 (June 2020), p. 112961. ISSN: 0045-7825. DOI: 10.1016/j.cma.2020.112961. URL: <https://www.sciencedirect.com/science/article/pii/S0045782520301444> (visited on 08/11/2022).

- [4] Caroline Hogue. “Shape representation and contact detection for discrete element simulations of arbitrary geometries”. In: *Engineering Computations* 15.3 (Jan. 1998). Publisher: MCB UP Ltd, pp. 374–390. ISSN: 0264-4401. DOI: 10.1108/02644409810208525. URL: <https://doi.org/10.1108/02644409810208525> (visited on 09/14/2022).
- [5] K. Karapiperis et al. “Stress transmission in entangled granular structures”. en. In: *Granular Matter* 24.3 (July 2022), p. 91. ISSN: 1434-7636. DOI: 10.1007/s10035-022-01252-4. URL: <https://doi.org/10.1007/s10035-022-01252-4> (visited on 09/02/2022).
- [6] Konstantinos Karapiperis, Jason P. Marshall, and José E. Andrade. “Reduced Gravity Effects on the Strength of Granular Matter: DEM Simulations versus Experiments”. EN. In: *Journal of Geotechnical and Geoenvironmental Engineering* 146.5 (May 2020). Publisher: American Society of Civil Engineers, p. 06020005. ISSN: 1943-5606. DOI: 10.1061/(ASCE)GT.1943-5606.0002232. URL: <https://ascelibrary.org/doi/full/10.1061/%28ASCE%29GT.1943-5606.0002232> (visited on 04/27/2022).
- [7] Konstantinos Karapiperis et al. “Investigating the incremental behavior of granular materials with the level-set discrete element method”. en. In: *Journal of the Mechanics and Physics of Solids* 144 (Nov. 2020), p. 104103. ISSN: 0022-5096. DOI: 10.1016/j.jmps.2020.104103. URL: <https://www.sciencedirect.com/science/article/pii/S0022509620303379> (visited on 04/27/2022).
- [8] Reid Kawamoto et al. “Level set discrete element method for three-dimensional computations with triaxial case study”. en. In: *Journal of the Mechanics and Physics of Solids* 91 (June 2016), pp. 1–13. ISSN: 0022-5096. DOI: 10.1016/j.jmps.2016.02.021. URL: <https://www.sciencedirect.com/science/article/pii/S002250961530154X> (visited on 12/06/2021).

- [9] Zhengshou Lai, Qiushi Chen, and Linchong Huang. “Fourier series-based discrete element method for computational mechanics of irregular-shaped particles”. en. In: *Computer Methods in Applied Mechanics and Engineering* 362 (Apr. 2020), p. 112873. ISSN: 0045-7825. DOI: 10.1016/j.cma.2020.112873. URL: <https://www.sciencedirect.com/science/article/pii/S0045782520300554> (visited on 09/14/2022).
- [10] Keng-Wit Lim and José E. Andrade. “Granular element method for three-dimensional discrete element calculations”. en. In: *International Journal for Numerical and Analytical Methods in Geomechanics* 38.2 (2014). eprint: <https://onlinelibrary.wiley.com/doi/pdf/10.1002/nag.2203>, pp. 167–188. ISSN: 1096-9853. DOI: 10.1002/nag.2203. URL: <https://onlinelibrary.wiley.com/doi/abs/10.1002/nag.2203> (visited on 12/06/2021).
- [11] Mohammad Mirkhalaf et al. “Toughness by segmentation: Fabrication, testing and micromechanics of architected ceramic panels for impact applications”. en. In: *International Journal of Solids and Structures* 158 (Feb. 2019), pp. 52–65. ISSN: 0020-7683. DOI: 10.1016/j.ijsolstr.2018.08.025. URL: <https://www.sciencedirect.com/science/article/pii/S0020768318303433> (visited on 11/16/2021).
- [12] John F. Peters et al. “A poly-ellipsoid particle for non-spherical discrete element method”. In: *Engineering Computations* 26.6 (Jan. 2009). Ed. by Antonio Munjiza. Publisher: Emerald Group Publishing Limited, pp. 645–657. ISSN: 0264-4401. DOI: 10.1108/02644400910975441. URL: <https://doi.org/10.1108/02644400910975441> (visited on 09/14/2022).